Aeronautics composite material inspection with a terahertz time-domain spectroscopy system

Frank Ospald
Wissem Zouaghi
René Beigang
Carsten Matheis
Joachim Jonuscheit
Benoit Recur
Jean-Paul Guillet
Patrick Mounaix
Wouter Vleugels
Pablo Venegas Bosom
Laura Vega González
Ion López
Rafael Martínez Edo

Aeronautics composite material inspection with a terahertz time-domain spectroscopy system

Frank Ospald,[a,*] Wissem Zouaghi,[b] René Beigang,[a] Carsten Matheis,[c] Joachim Jonuscheit,[c] Benoit Recur,[d] Jean-Paul Guillet,[e] Patrick Mounaix,[e] Wouter Vleugels,[f] Pablo Venegas Bosom,[g] Laura Vega González,[g] Ion López,[g] Rafael Martínez Edo,[h] Yehuda Sternberg,[i] and Marijke Vandewal[j]

[a]University of Kaiserslautern, Department of Physics and Research Center OPTIMAS, Erwin-Schroedinger-Strasse 56, 67663 Kaiserslautern, Germany
[b]Johann Wolfgang Goethe University, Institute of Physics, Max-von-Laue-Strasse 1, 60438, Frankfurt am Main, Germany
[c]Fraunhofer Institute for Physical Measurement Techniques IPM, Department of Materials Characterization and Testing, Erwin-Schroedinger-Strasse 56, 67663 Kaiserslautern, Germany
[d]Bordeaux 1 University, LaBRI, CNRS UMR 5800, 351 cours de la Libération, 33405 Talence, France
[e]Bordeaux 1 University, LOMA, CNRS UMR 5798, 351 cours de la Libération, 33405 Talence, France
[f]Verhaert New Products and Services, Hogenakkerhoekstraat 21, 9150 Kruibeke, Belgium
[g]Centro de Tecnologías Aeronáuticas, C/Juan de la Cierva, 1, Parque Tecnológico de Álava, 01510 Miñano, Álava, Spain
[h]LGAI Technological Center S.A., Campus UAB, 08193 Bellaterra, Barcelona, Spain
[i]Israel Aerospace Industries, NDT Laboratory, Engineering Division, Ben-Gurion International Airport, 70100 Tel Aviv, Israel
[j]Royal Military Academy, CISS Department, Av. de la Renaissance 30, 1000 Brussels, Belgium

Abstract. The usability of pulsed broadband terahertz radiation for the inspection of composite materials from the aeronautics industry is investigated, with the goal of developing a mobile time-domain spectroscopy system that operates in reflection geometry. A wide range of samples based on glass and carbon fiber reinforced plastics with various types of defects is examined using an imaging system; the results are evaluated both in time and frequency domain. The conductivity of carbon fibers prevents penetration of the respective samples but also allows analysis of coatings from the reflected THz pulses. Glass fiber composites are, in principle, transparent for THz radiation, but commonly with significant absorption for wavelengths >1 THz. Depending on depth, matrix material, and size, defects like foreign material inserts, delaminations, or moisture contamination can be visualized. If a defect is not too deep in the sample, its location can be correctly identified from the delay between partial reflections at the surface and the defect itself. © *The Authors. Published by SPIE under a Creative Commons Attribution 3.0 Unported License. Distribution or reproduction of this work in whole or in part requires full attribution of the original publication, including its DOI.* [DOI: 10.1117/1.OE.53.3.031208]

Keywords: composite materials; terahertz imaging; non-destructive testing; carbon fiber reinforced plastic; glass fiber reinforced plastic; honeycomb; Rohacell; laminate.

Paper 131243SS received Aug. 14, 2013; revised manuscript received Oct. 11, 2013; accepted for publication Oct. 28, 2013; published online Dec. 16, 2013.

1 Introduction

The desire to simultaneously fulfill the seemingly contradicting requirements of reduced weight and enhanced stability drives the development of sophisticated, complex, and heterogeneous composite materials. The aircraft industry, both civilian and military, naturally is a key player in this field. The advancement of materials calls for correspondingly advanced methods and technologies for inspection and failure detection during production or maintenance, especially in the area of nondestructive testing (NDT). A wide range of NDT techniques has been established and matured; however, a silver bullet method that can identify all kinds of defects and failure modes with equally high precision does not yet exist. THz spectroscopy, imaging, and tomography,[1–8] on the other hand, are becoming increasingly attractive tools for NDT purposes, since THz radiation penetrates most nonmetallic and nonpolarized media, can be applied contact-free, and does not require special safety precautions like radiographic imaging. THz NDT on aeronautics materials first came to the limelight with the inspection of space shuttle isolation foam after the 2003 Columbia accident[9] and has since been applied

to various NDT tasks on aeronautics materials and coatings. This includes ceramics,[10] glass fiber composites[11,12] as well as surface roughness and corrosion of metal under coatings.[13,14] Conductive materials like metal or carbon fibers are excellent THz reflectors, which commonly limits the applicability of THz radiation to surface defects for these cases. Reflectance and transmittance in carbon fiber sheets, however, depend on the orientation of the fibers with respect to the polarization of the THz radiation: Not unlike in a wire-grid polarizer, THz radiation which is polarized perpendicularly to the fibers experiences a higher transmittance than for parallel polarization. The anisotropic THz characteristics of carbon fibers have been utilized to examine heat damage[15] as well as delamination[16] at or close to the surface. There are numerous further examples of THz methodologies and applications in NDT of composites. An extensive review is given in Ref. 17.

The project DOTNAC (Development and Optimization of THz NDT on Aeronautics Composite Multilayered Structures; http://www.dotnac-project.eu) aims for the development of a fast, high resolution, noninvasive, and noncontact inspection tool for assessing aeronautic composite parts either during production or maintenance on the basis of THz radiation. It is carried out by a consortium of 10

---

*Address all correspondence to: Frank Ospald, E-mail: ospald@physik.uni-kl.de

partner institutions that include research organizations, NDT specialists, and aircraft manufacturers. The tool should be easy to integrate into industrial facilities and fill performance gaps present in existing NDT methods. It is therefore expected to be a complimentary technique with the potential to be more precise for certain kinds of defects and/or structures. The assessment of that potential and the performance of THz material inspection are essential parts of the project. All THz measurements will therefore be compared to reference data taken with established NDT techniques, such as ultrasound, radiographic testing, and infrared thermography, to deliver a THz feasibility study for the inspection of aeronautics composite materials.

DOTNAC takes a two-pronged approach to deliver a more comprehensive picture of the THz capabilities on aeronautics composite materials: both a frequency-modulated continuous wave (FMCW) and a pulsed time-domain spectroscopy (TDS) system are set up and used for the inspection of a broad range of typical samples. While both systems are designed to work as stand-alone devices, they possess portable sensors that can be operated remotely via a cable harness in a three-dimensional (3-D) scanner working in reflection mode, which is the third hardware component developed in the project. This scanner unit can alternately incorporate the FMCW or TDS sensor and capture data on a nonflat part, specifically a test radome (see Fig. 1). The functionality and performance of the FMCW tool are described elsewhere;[18] a brief overview is given in Sec. 3.1.

In the main part of the article, we will first give an overview of the various sample types that have been manufactured for the project. Next, we will explain the two THz-TDS systems from which data are presented here. Besides the mobile fiber-coupled DOTNAC TDS tool, we use a laboratory system installed at the TeraTec application center of Fraunhofer IPM as a reference system. These descriptions are followed by a presentation of our imaging results. An assessment of the potential of THz-TDS for aeronautics NDT and an outline of possible further developments conclude this study.

2 Samples

Two general categories of composite structures are available for investigation with pulsed THz radiation: glass fiber reinforced plastic (GFRP) and carbon fiber reinforced plastic

(CFRP). While the relevance of CFRP for the construction of aircraft is ever growing, especially for high-performance components, its conductivity is an inevitable obstacle to penetration with THz radiation. In tests conducted by ourselves, the transmitted THz amplitude in the case of perpendicular polarization was 11 times higher than for parallel polarization on a single-carbon fiber sheet but still very low compared to the incident signal (1.2% of the incident amplitude was transmitted for perpendicular polarization compared to 0.11% for parallel). In a set of samples with impact-damaged CFRP panels with 5 mm thickness, for example, the deformation of the surface by the impactor could be visualized as a dent, but the critical crack formation inside the sample is invisible to THz inspection. On the other hand, the good THz reflectivity of CFRP enables the inspection of coating layers on CFRP substrates.

The GFRP samples are either solid laminates, consisting of several plies, or sandwich structures that incorporate one (A-sandwich) or two (C-sandwich) cores between GFRP skins. Two kinds of sandwich cores are used: Rohacell foam and a honeycomb structure. The samples further differentiate into samples with artificial, well-defined defects (so-called "calibration samples") and such with defects created through intentional faults in their fabrication process (test samples). The calibration samples include rectangular inserts serving as mock defects, water contaminations of different volumes and impact damages with various kinetic energies. The test samples include debonds and delaminations as well as a sample with enhanced porosity level. The misprocessed coatings on CFRP panels are also classified as test samples. Figure 2 summarizes the selection of samples.

3 THz Imaging Systems

3.1 FMCW Setup

For the sake of completeness, the key parameters of the complimentary, fully electronic FMCW system should be mentioned. This tool employs interchangeable transceiver heads whose frequency ramps are operated via a voltage-controlled oscillator, a frequency multiplier chain, and a Schottky diode mixer for heterodyne detection each. Three sensors with center frequencies of 100, 150, and 300 GHz and corresponding output powers of 2, 0.1, and 0.06 mW were used. Another high-frequency measurement head at 850 GHz (2 μW output power) was found not to have sufficient

Fig. 1 The DOTNAC three-dimensional (3-D) scanner platform; schematic drawing with mounted FMCW sensor head (a), photograph of mounted TDS sensor and test radome (b).
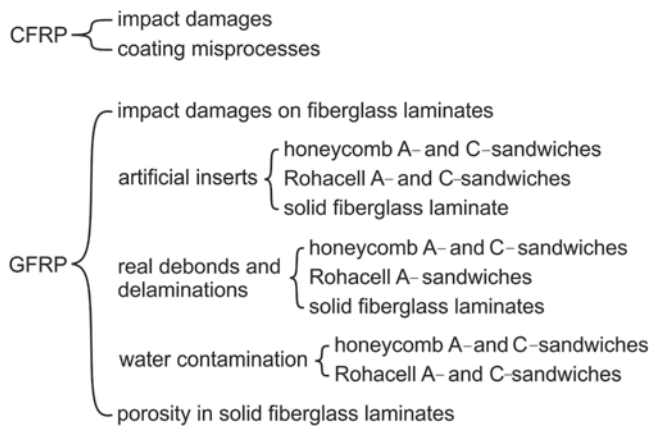
Fig. 2 Overview of the sample structures and defect types available in DOTNAC.

Fig. 3 Top view of time-domain spectroscopy (TDS) reference setup for reflection measurements. The THz beam is guided in a dry air enclosure.

penetration capability on the samples for satisfactory imaging results. The sensors were operated both in focused and synthetic aperture geometry; furthermore, datasets from the 100 and 150 GHz heads could mathematically be fused together into an ultra-wideband frequency range to create a virtual sensor that combines the relatively high material transparency at low frequencies with enhanced depth resolution through a broadband frequency ramp.

3.2 TDS Reference Setup

The samples described above should be examined not only with the mobile TDS tool that will be presented in the next section, but also with a reference system with well-known specifications and proven performance. The aim for the reference measurements is the acquisition of high-quality THz images to analyze the general potential and limitations for composite materials' inspection. For this purpose, we used a stationary TDS raster scan imaging system with InAs surface emitter and LTG GaAs photoconductive antenna detector. Both are pumped in a free-space setup by a Ti:Sa laser at 800-nm center wavelength; the THz beam is guided in a dry air enclosure to suppress water absorption features in the data. The time delay between pump and probe pulse is varied with a shaker that oscillates at 10 Hz, so that effectively 20 data traces/s are recorded, since the data from both half-cycles of the shaker motion are captured and one set afterward is mirrored in the time domain. The use of the shaker limits the available bandwidth to 2 THz, with the center frequency being at 500 GHz. The area raster scan algorithm moves the sample horizontally at 1 mm/s velocity through the THz focus at perpendicular incidence and takes data in on-the-fly mode. At the end of a line scan, the sample is moved by a vertical increment of 0.1 mm and the next line scan, in reverse direction, is started. Oversampling is done both in horizontal and vertical directions. This results in high-resolution images and requires 30 h for a $100 \times 100 \text{ mm}^2$ area at the reference settings. The setup can be used in reflection or transmission geometry; if not stated otherwise, the data shown in this article have been taken in reflection geometry (see schematic in Fig. 3) to match the mode of operation of the 3-D scanner demonstrator, which was built in the DOTNAC project.

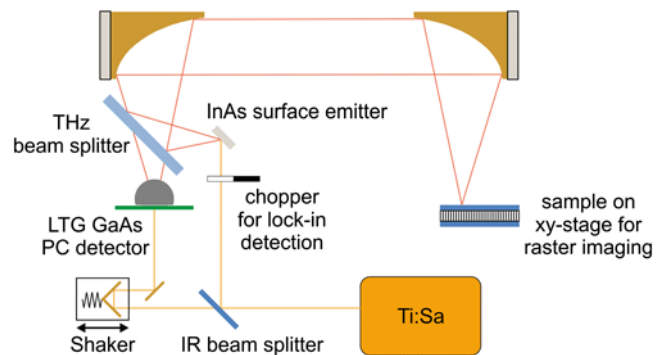The datasets taken in this way contain a time-domain trace of the electric field for every pixel, so that they are effectively four-dimensional (x, y, time, amplitude). After applying a Fourier transform, the corresponding frequency information is available. The images were manually evaluated in the time and frequency domain by browsing through the datasets along the time or frequency axis, comparable to a flip-book. Additionally, a "static" image, which displays the time-domain peak-to-peak (p2p) amplitude value for each pixel, was examined. Examples for the evaluation modes are given in Fig. 4.

The reflection peak from the sample surface is the dominating feature for most of our samples. As a consequence, the p2p images mainly probe that surface, i.e., only if a defect in the sample has an effect on the surface like a bulge that reduces reflection at its slopes, it can be visualized with the p2p mode.

The delay evaluation naturally is suited to discover defects hidden in the volume of the sample by identifying local discontinuities in the dielectric behavior that cause in- or decreased reflection and/or absorption, respectively, which manifest themselves as trailing peaks at various time delays. Depth information about features that are generated within a sample, e.g., partial reflection at a discontinuity, can be calculated from the time-of-flight difference between the surface reflection and the feature of interest. This requires information about the THz dielectric function of the sample or at least the average refractive index between ~0.1 and 1 THz. The lower end of this range is given by the system characteristics, the upper by the materials under test themselves. Preliminary examinations gave a high THz opacity beyond 1 THz for virtually all materials that have been tested in DOTNAC, which restricts the penetrability of the samples with broadband radiation. This also limits the detectability of defects that are embedded deep in a sample.

The frequency spectrum of the main surface reflection pulse is modulated by trailing pulses which are generated at defects in the sample volume and can therefore also be used to discriminate between pristine material and embedded defects. However, small trailing pulses from interfaces in the sample will cause correspondingly small oscillations in the spectrum. Additionally, interference effects might manifest themselves in the frequency images and block spectral windows from analysis. Laminate samples contain by definition multiple internal interfaces between their constituting plies and hence exhibit a multitude of reflections which complicate defect identification.
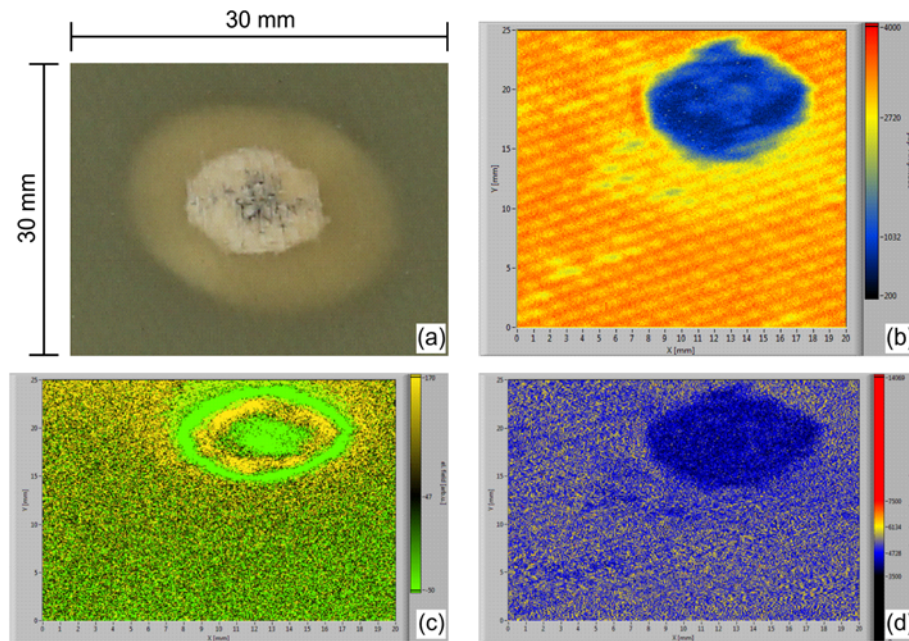
Fig. 4 Example for the evaluation modes of the TDS reference system. Top row: photograph detail (a) and corresponding THz p2p image (b) of rear side of GFRP laminate panel impacted with 30-J energy. The impact on the front side causes a bulge on the rear, leading to a reduced THz reflectivity over the whole impact area. Bottom row: defect visualized in the time (c) and frequency domain (d); pictures at different delay times allow a deeper analysis of the defect structure, whereas the frequency evaluation here is very similar to the p2p image. The plots in the remainder of the paper are shown without the linear color scale bars, since only the visual contrast was used to assess the detectability of a defect.

3.3 DOTNAC TDS Setup

The concept for the DOTNAC project TDS system follows several key specifications, which arise from its purpose as a demonstrator for an industrial grade system that should be suitable for usage on the shop-floor and could be integrated into testing facilities. As such, robustness, flexibility, and speed are issues to be addressed. It is desirable to construct a rigid system that requires a minimum of readjustment after long-distance transport by employing as many fiber optical (in contrast to free-space) components as possible. This coincides with the need to provide remote sensors that can be operated via electrical cables and fiber optical patchcords over a distance of at least 5 m from a base unit, to allow for the motion of the sensors on the five axes (X, Y, Z, θ, ψ) 3-D THz scanner. Finally, the system should be able to scan a time-domain trace of at least 100 ps in at most 10 ms, that is to say at a data acquisition rate of 100 Hz.

These parameters differ significantly from the design goals of the reference system, which provides THz imaging with high quality at the expense of being complex, immobile, and limited in data acquisition speed. As an adequate response to the DOTNAC project requirements, a fiber-integrated electronically controlled optical sampling (ECOPS) setup was chosen. It consists of two nominally identical pulsed fiber lasers with 1560-nm center wavelength and 74.5-MHz repetition rate, which emit pulses of 100 fs duration and 70 mW average power at the end of a 6-m-long fiber delivery (customized versions of the FemtoFErb model by TOPTICA Photonics, 82166 Graefelfing, Germany). A phase-locking electronics module allows synchronizing the cycle of the slave with that of the master laser so that their pulses are emitted with a fixed time delay. Alternatively, the delay can be varied by applying a voltage

to a phase shifter input, which modifies the repetition rate of the slave laser until a time delay has built up that corresponds to the applied voltage.[19] We chose a sinusoidal waveform, effectively generating an analogous time delay variation to that caused by an optomechanical shaker. Therefore, for each cycle of the modulation voltage, two THz traces can be recorded, one on the half-wave with a positive slope and one on that with a negative slope. Figure 5 shows a sketch of the main system components.

The ECOPS operating principle is very similar to the well-known asynchronous optical sampling (ASOPS) technique; the principal difference is that ASOPS works with a fixed repetition rate detuning of the slave laser, whereas ECOPS employs a variable one. In ASOPS, the time delay between the laser pulses thus grows in each cycle by
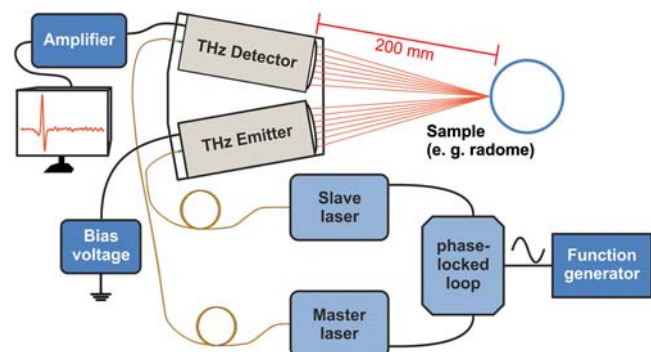

Fig. 5 Schematic depiction of the basic elements of the DOTNAC TDS system setup. The sensor heads are mounted in specular reflection geometry for 10 deg angle of incidence to the sample surface normal. The time delay variation does not require a mechanical delay stage due to the voltage-controlled phase shift between master and slave laser.
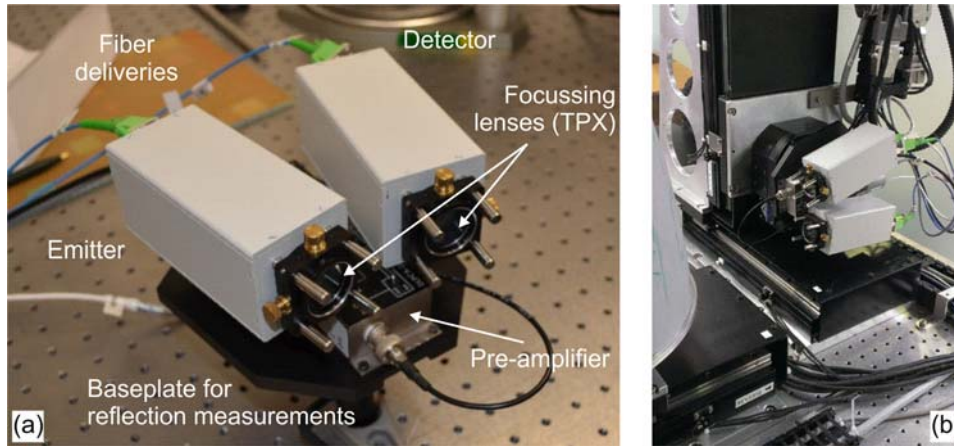
Fig. 6 The DOTNAC TDS sensor assembly mounted on a post (a) and vertically on the 3-D scanner motion platform (b).
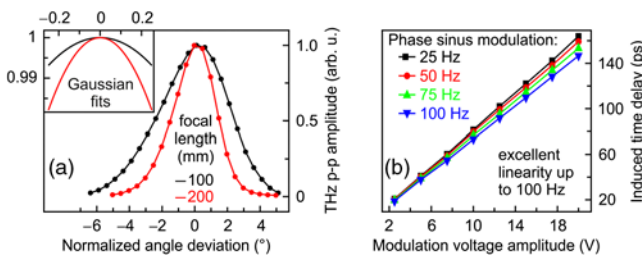

Fig. 7 (a) Measured decrease of THz reflectance with deviation from nominal angle for specular reflection for lenses with 100 and 200 mm focal length. The relative positioning accuracy of sensor and sample surface with respect to each other should limit the deviation from specular reflection conditions to ± 0.2 deg at all times during a measurement to capture 99% of the maximum signal amplitude (see inset). (b) Linear response of ECOPS control loop within the targeted parameter space. 20 V is the maximum allowed modulation peak voltage for continuous operation according to manufacturer specifications.

Fig. 8 (a) Photograph detail of front (impact) side of GFRP laminate panel with 15 (top right) and 22 (bottom left) J impact energy. (b) Corresponding THz p2p image with linear color scale; the lower energy impact (black arrow) can hardly be identified, but the other one can due to the reduced reflectivity at its slopes.

the increment determined through the repetition rate difference so that the pulses overlap in time again after the total delay has added up to the inverse of the master laser repetition rate. The time window that is captured, hence, corresponds to this. For common mode-locked fiber lasers, typical repetition rates are on the order of 100 MHz, which creates datasets of 10 ns length. The information of a THz trace, however, is in most cases contained in ~100 ps so that up to 99% of an ASOPS dataset are junk data that do not include relevant information. The variable time delay of ECOPS allows one to limit the captured THz traces to meaningful information and thus enables a more efficient data acquisition. Note that these statements are made for a setting where the distance from sensor to target, and in this way the zero delay offset, is kept virtually constant. This is realized in our measurements and would also apply to other arrangements that utilize focusing optics and require the targets to stay within a Rayleigh length of a few millimeters. For a stand-off scenario, possibly with moving targets, the wide time delay window of ASOPS would be advantageous or even necessary.

Our sensor consists of two fiber-coupled measurement heads that include photoconductive antennas as emitter and detector of THz radiation and TPX lenses for beam shaping. The measurement heads are mounted under an angle of 20 deg on a baseplate which can be attached to the 3-D
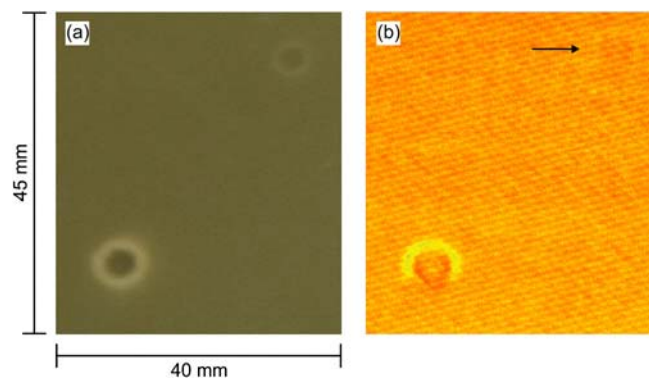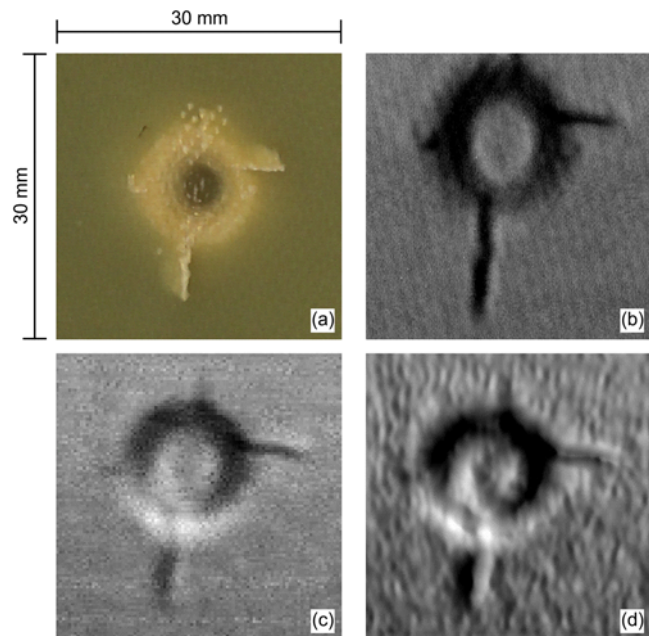

Fig. 9 Top row: photograph detail (a) and corresponding THz p2p image from reference system (b) of front side of GFRP laminate panel impacted with 40-J kinetic energy. Bottom row: defect captured with the mobile DOTNAC TDS system; raw data p2p image (c) and postprocessed pseudo-3D image for contrast enhancement (d).
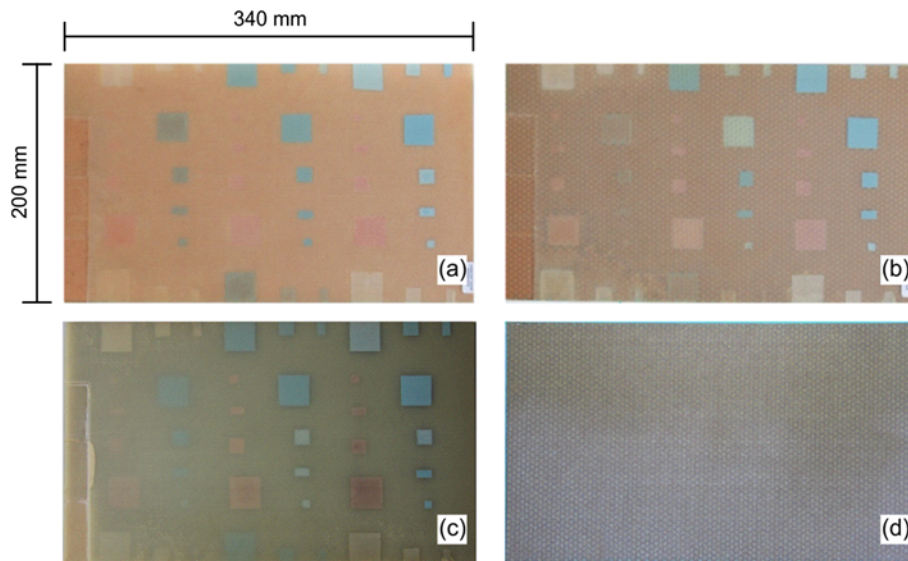
Fig. 10 Photographs of a selection of calibration samples with inserts serving as artificial defects: airgaps (white), polyethylene (blue), and Teflon (red). Top row: A-sandwich panels with Rohacell (a) and honeycomb (b) core. Bottom row: 20-ply solid laminate (c) and honeycomb core C-sandwich (d).

scanner unit, alternatively to an FMCW transceiver head (see Fig. 6). The focal distance of the THz optics is 200 mm to match the working distance of the scanner. The focusing lenses can easily be dismounted to allow the use of other optics, for example, with sharper focusing for enhanced spatial resolution. Also mounted on the baseplate is a trans-impedance amplifier for signal preprocessing. With the maximum specified phase offset modulation voltage, our ECOPS system can scan a time window of 146 ps at 100-Hz modulation frequency. This range is calibrated with a nonlinear frequency-doubling crystal on which the beams of master and slave laser are collinearly overlapped. Note that within our measurement accuracy, the delay–voltage response at 100 Hz is still linear, with only a small decrease of the maximum scan range compared to lower modulation frequencies [see Fig. 7(b)]. At higher frequencies approaching 1 kHz, the hysteresis of the piezo actuator that modulates the repetition rate of the slave laser would lead to a saturation of the delay range at lower voltages.

4 Results

The majority of the results presented in the following sections have been measured with the reference system since the optimization of the mobile system and the taking of data with it are still ongoing. This section, therefore, aims to present a broad overview about the potential of THz-
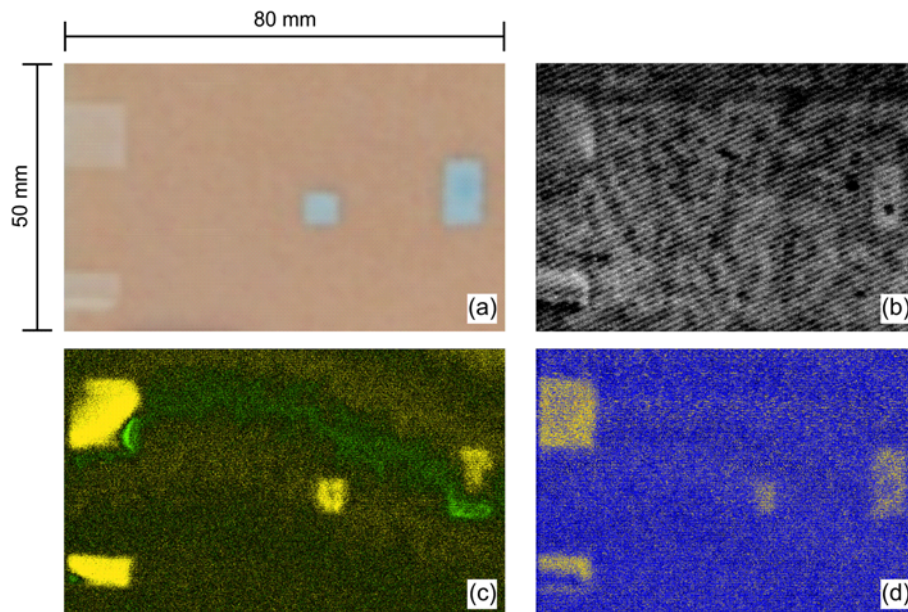

Fig. 11 Top row: Photograph detail (a) and THz p2p (b) image of Rohacell A-sandwich with embedded airgaps (white rectangles, left part of sample) and polyethylene sheets (blue rectangles, right part of sample) approximately 0.5 mm below the surface. Bottom row: Corresponding delay (c) and frequency (d) images.
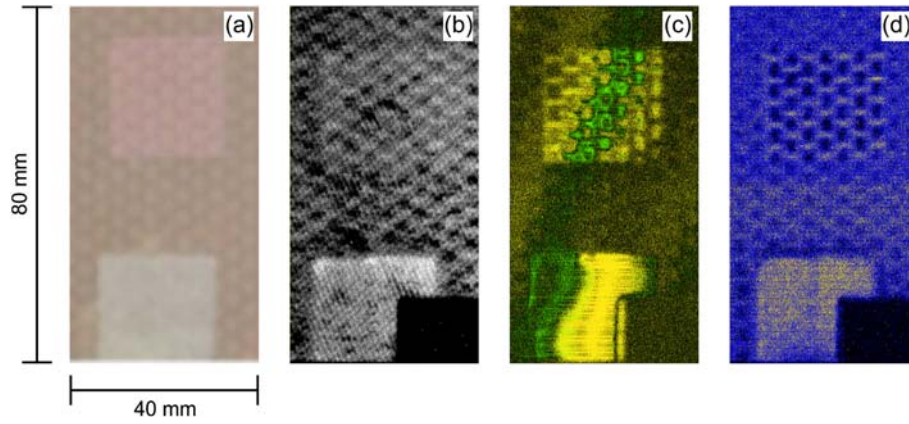
Fig. 12 Photograph detail (a) of honeycomb A-sandwich with embedded airgap (white rectangle, bottom) and Teflon sheet (red rectangle, top) approximately 0.5 mm below the surface. Corresponding p2p (b), delay (c) and frequency (d) images. The bottom right area of the panel is covered by the sample holder.

TDS for the analysis of aircraft composite materials. Data from the DOTNAC TDS system, when available for comparison, are shown and explicitly denoted.

4.1 Impact Damages

GFRP laminates panels, which had been mechanically damaged with four different impact energies between 15 and 40 J, were investigated. Albeit being visible, the impact with the lowest energy could not be identified in the THz images, as can be seen in Fig. 8. The other three impacts with energies of 22, 30, and 40 J could all be detected (see Figs. 8 and 9). While p2p and frequency images highlight the slopes of an impact damage where the back
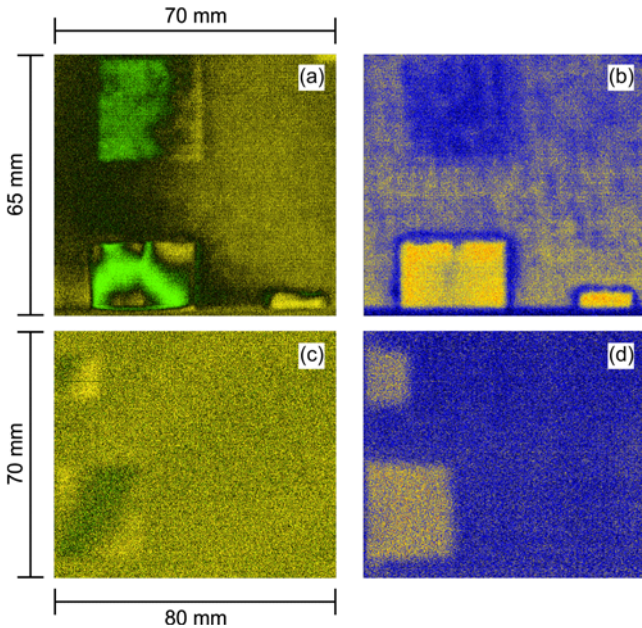

Fig. 13 Time (a and c) and frequency (b and d) domain images from 20-ply laminate panel with defects 0.5 mm below front surface. Top row: front surface with two airgaps at the image bottom and a Teflon square at the upper left. The quadratic shape of the airgaps in (a) and (b) is cropped by the sample holder. Bottom row: same field of view from the rear side (rotated by 90 deg); the defects are now 4.5 mm below the surface. Only the airgaps can be visualized at this depth.
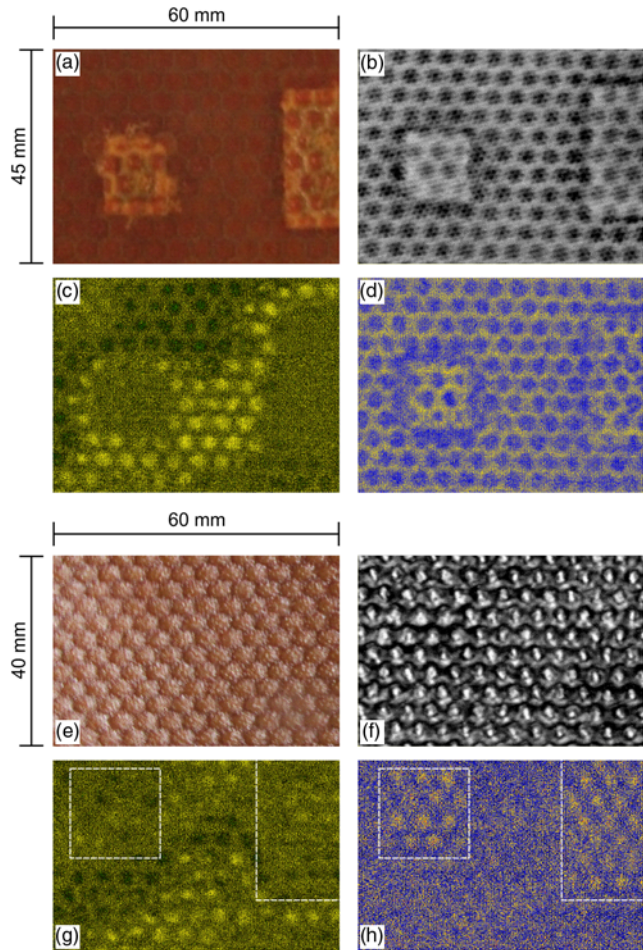

Fig. 14 Top row: photograph (a) and THz p2p image (b) of honeycomb core A-sandwich patch with debonds between skin and adhesive sheet approximately 0.75 mm below front surface. Second row: Corresponding delay (c) and frequency (d) images. Delay is at 71 ps below surface, i.e., after reflection at the back of the core; frequency is 691 GHz. Third row and bottom row: same field of view, but from the rear side of the sample. Whereas the p2p image (f) does not allow identification of the defects, the delay (g) and frequency (h) evaluations still reflect the presence of the defects: The time-domain wavefront visible in the lower part of (g) is distorted at the debond sites (indicated with white dashed rectangles), while (h) shows a slight contrast difference in the frequency domain. Delay time is ~68 ps below rear surface, frequency at 290 GHz.

reflection is reduced, the delay image can additionally identify compression of material or delaminations caused by mechanical shock.

4.2 Artificial Inserts

To simulate foreign inclusions, debonds, and delaminations, five GFRP panels (one laminate, plus one A-sandwich and C-sandwich each with Rohacell and honeycomb cores, respectively) with artificial inserts as mock defects were fabricated. Each contains 42 rectangular inserts ranging from 6×6 to 25×25 mm^2 that are patterned in three different depths within the samples. In the laminate sample made of 20 plies, the inserts are placed between the second and third, fifth and sixth, and tenth and eleventh ply, i.e., at 10%, 25%, and 50% of the total thickness. A single ply is ~0.25-mm thick. A-sandwiches have the inserts within the four-ply top skin, between the top skin and the adhesive which bonds it to the core and between this adhesive and the core, so that all defects are placed on one side of the core, which is defined as the front side. The C-sandwich structures have the defects centered in the middle six-ply skin between the two cores, between the central skin and the adhesive bonding it to the front side core and between that adhesive and the core, respectively. Each insert group consists of airgaps, polyethylene, and Teflon patches. Examples are shown in Fig. 10.

In general, the detectability scales down with increasing depth and also depends on the material of the inserts. Airgaps yield the highest contrast due to the maximum difference in refractive index with the host material (2.07 is typical for fiberglass plies), whereas polyethylene and Teflon, commonly
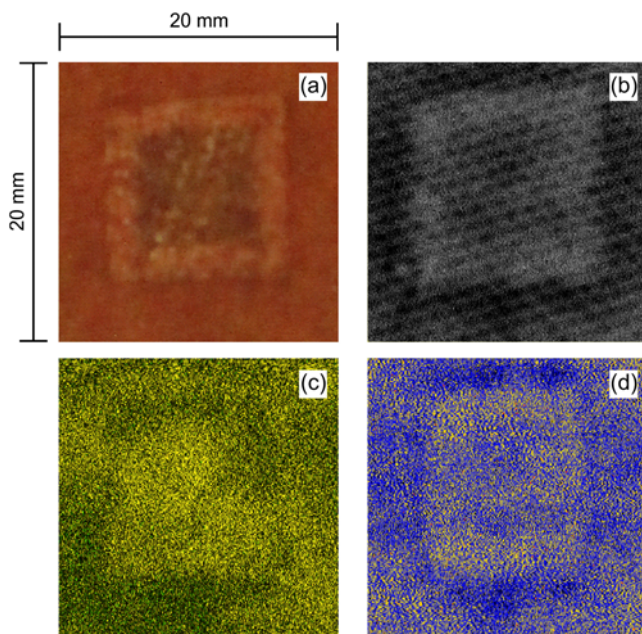
having THz refractive indices around 1.5 and THz transmittance around 90%, are harder to identify. This applies especially when they are close to or embedded in adhesive, which was measured to have a THz refractive index around 1.6, so their visibility diminishes. Furthermore, in general, the best defect identification could be done in delay evaluation and slightly worse in frequency mode, whereas p2p images are only useful for airgaps. Examples for measurements on A-sandwich front sides are shown in Fig. 11 (Rohacell) and in Fig. 12 (honeycomb), whereas Fig. 13 presents a comparison of data from front and rear sides of the laminate panel.

Regarding sandwich structures, there is a significant difference in the response caused by the core material: While both Rohacell and honeycomb cores have an average refractive index close to 1 in the lower THz band (~1.02 to 1.05) and are thus expected to have similar reflection characteristics, the attenuation in transmission is almost an order of magnitude higher for Rohacell. We measured an absorption coefficient between 0.24 and 0.32 mm^{-1} for Rohacell and only 0.039 mm^{-1} for honeycomb cores. In our C-sandwich samples, the inserts, debonds, and delaminations are positioned close to the center between the two cores. THz radiation that reflects at such a defect, therefore, must traverse a core twice on the way from emitter to detector. This limits the detectability already a lot in honeycomb C-sandwiches, and even more in Rohacell sandwiches. In fact, we could hardly detect these defects in Rohacell C-sandwiches at all; for the same reason, detection on Rohacell A-sandwiches was almost impossible from the rear side when the central (single) core is between the defect and the sensor. We suspect scattering in the foam matrix as the main reason for the high THz opacity of Rohacell. For honeycomb C-sandwiches, the deep defects leave traces in the delay images to some extent. For that reason, the inspection of honeycomb
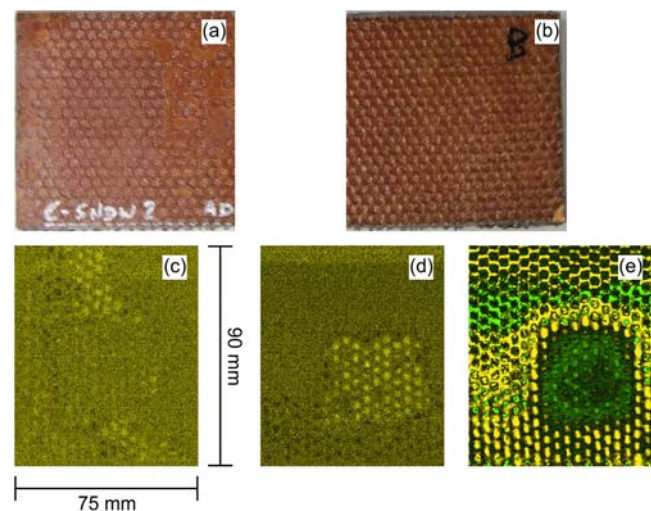

Fig. 15 Top row: photograph (a) and THz p2p image (b) of Rohacell core A-sandwich patch with debond between skin and adhesive sheet approximately 0.75 mm below front surface. Bottom row: corresponding delay (c) and frequency (d) images. Delay is at 7 ps below surface; frequency is 640 GHz. The core thickness of 9.5 mm prevents measurements from the rear side because of its strong THz opacity (compare with Fig. 14).

Fig. 16 Top row: photographs of front (a) and rear (b) side of honeycomb core C-sandwich patch with debond between inner adhesive and core approximately 10.3 mm below front surface. Bottom row: Time-domain images from front (c) and rear side (d) at roughly 70 ps delay from the respective surface, which corresponds to the actual depth of the defect. (e) Delay image close to rear surface, showing a strong effect of the debond more than 10 mm below.
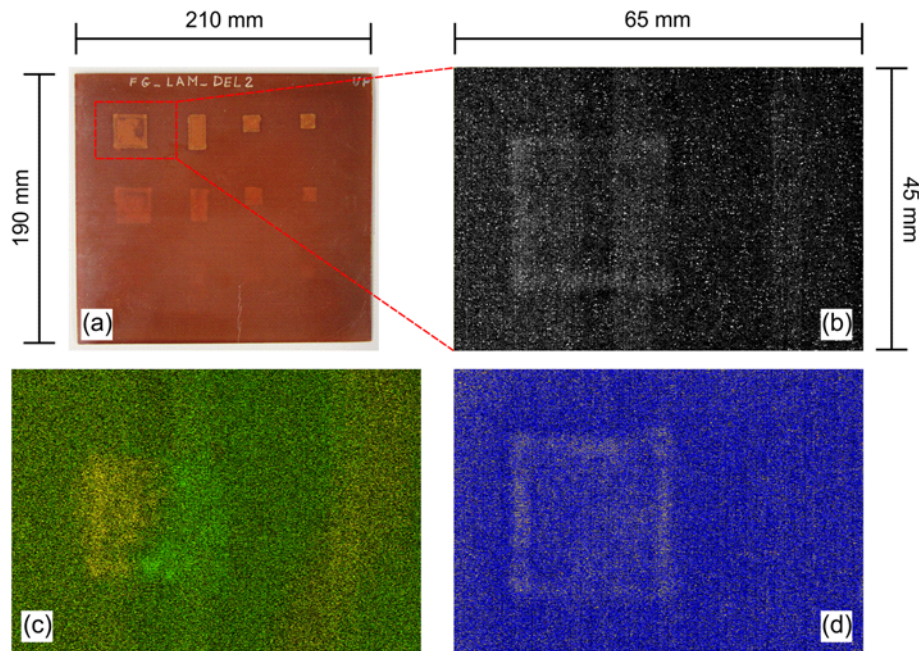
Fig. 17 Top row: front side photograph (a) and THz p2p image (b) of upper left corner of solid laminate (20 plies) including delaminations at different depths. Bottom row: (c) corresponding delay image at 8 ps; the defect is ~0.5 mm below the front surface. (d) Corresponding frequency image at 551 GHz.

A-sandwiches from the rear is best done in delay mode. Note, however, that the measurements were performed with tight focusing for high lateral resolution so that in C-sandwiches with more than 10 mm thickness, the beam divergence beyond the focal area is problematic. By changing to optics with a wider beam waist, but longer Rayleigh length, reflections from the whole sample volume can be captured.

4.3 Debonds and Delaminations

The utilizability of THz-TDS was then tested on several A-sandwiches which contain debonds (both Rohacell and honeycomb core), honeycomb C-sandwiches with debonds or delaminations, as well as solid fiberglass laminates that include delaminations. The A-sandwiches show a similar behavior as their calibration counterparts: detectability in
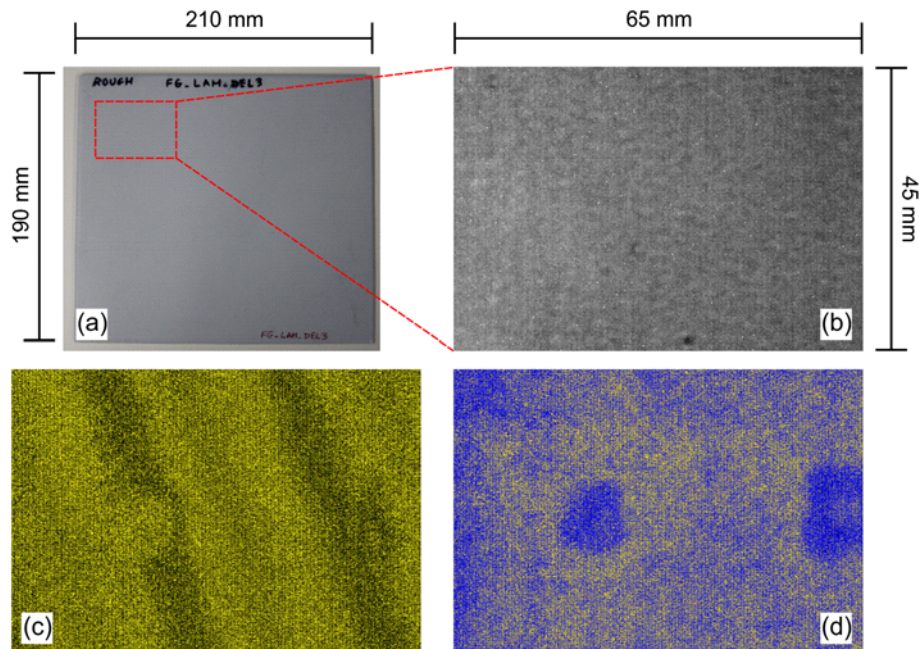

Fig. 18 Top row: front side photograph (a) and THz p2p image (b) of upper left corner of solid laminate (20 plies) including delaminations at different depths. Compared to the sample of Fig. 17, this sample has the defect arrangement rotated by 180 deg and a polyurethane coating which prevents defect identification in p2p mode. Bottom row: (c) corresponding delay image at 33 ps. Because of the different defect arrangement, this defect is smaller and deeper in the sample (2.5 mm), and a neighboring defect at the right frame edge is visible. (d) Corresponding frequency image at 551 GHz.
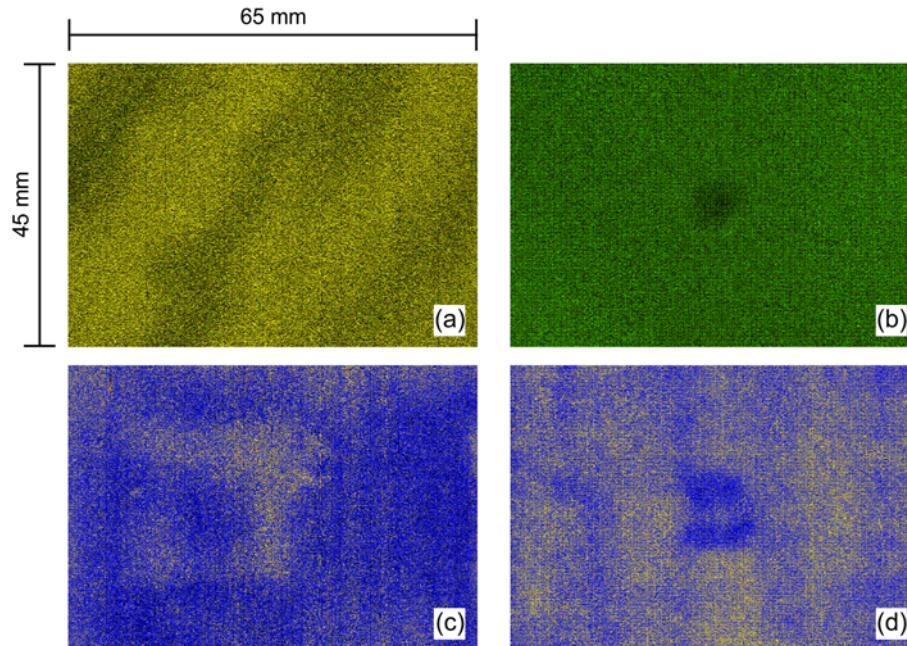
Fig. 19 Images of above defects (Figs. 17 and 18) from the rear side, rotated by 90 deg. Top row: Delay images at 31 ps (a) and 33 ps (b). The delay in (a) does not correspond to the actual depth of the defect below the rear surface, which would be ~70 ps. This layer is inaccessible for direct visualization because of dispersion and absorption; instead, the bulging of a ply closer to the rear surface due to the delamination underneath is weakly visible. Bottom row: corresponding frequency images (c and d), both at 551 GHz. The second defect which is visible in Fig. 18 (c and d) is not in the observation window of Fig. 19 (b and d).

general is good from the front side and still possible from the rear side when the sample contains a honeycomb core, but degrades for a Rohacell core. In fact, detection from the rear side was not possible on the Rohacell test sandwiches. Figure 14 displays THz images from front and rear side of an A-sandwich with avhoneycomb core, whereas Fig. 15 shows data from a Rohacell core A-sandwich (front side only).

C-sandwich test samples gave lower contrast in THz-TDS compared to the A-sandwiches, as was expected from the calibration samples. Only larger defects could be detected via time-domain evaluation, as can be seen in Fig. 16.

The three fiberglass solid laminates had delaminations placed at 0.5, 1.25, and 2.5 mm depth below the front surface, like in the calibration laminate with inserts. Airgaps,
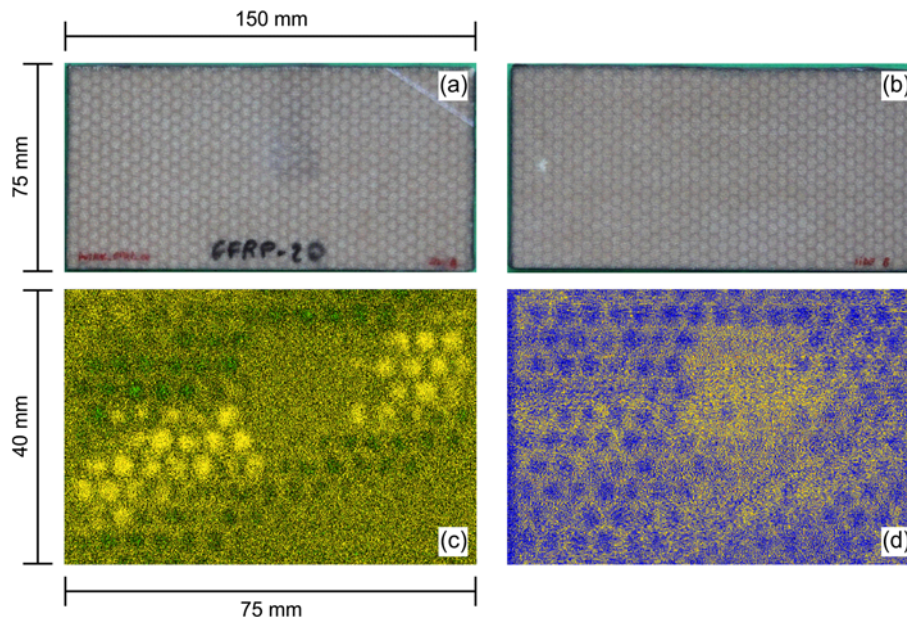

Fig. 20 Top row: photographs of honeycomb core C-sandwich, (a) surface close to water-injected core, (b) surface close to pristine core. The water contamination (0.75 ml) is visible from the corresponding side [dark area in picture (a)]. In A-sandwiches, the patch of moisture is visible from both sides. Bottom row: delay (c) and frequency (d) THz images of front side central area (rotated by 90 deg).
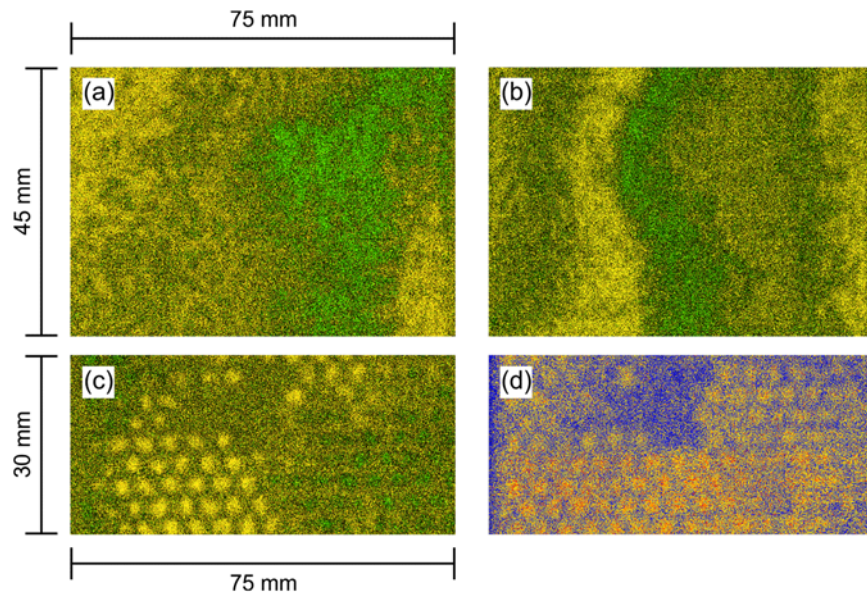
Fig. 21 Top row: delay images ~0.5 mm beneath the surface at 7 ps time delay of Rohacell A-sandwich with 0.75 ml water content in the core; front (a) and rear (b) side. The water causes a distortion of the wavefronts. Bottom row: delay (c) and frequency (d) THz images from front side of honeycomb A-sandwich with 0.75 ml water content in the core. Enhanced absorption after reflection at the back of the core (at 40 ps delay) makes the contamination visible in both domains (frequency is 373 GHz).

i.e., mock delaminations, were almost the only inserts in the calibration sample that gave a weak contrast in the p2p images. In the test samples, the detection rate in p2p is even lower (probably because a real delamination is a weaker damage than an airgap created with a blade) and negligible. One of the test samples has a polyurethane (PU) coating that prohibited any detection in p2p mode. Delaminations in the test fiberglass solid laminates could be detected in delay and frequency evaluation, however, with lower contrast than in the calibration sample. Even when measuring from the rear side, the deepest defects at 4.5 mm below the surface could be spotted. Data from fiberglass laminates are presented in Figs. 17–19.

4.4 Water Contamination

Samples with three different volumes of water contamination were fabricated (0.2, 0.35, and 0.75 ml). For each set of volumes, A- and C-sandwiches with Rohacell and honeycomb cores were available so that we inspected 12 samples in total. The water was injected into the core of the A-samples and one of the C-sandwich cores, respectively. Therefore, the contamination in the C-sandwiches was only identifiable from the sample surface which is closest to that core. Measurements from a honeycomb core c-sandwich are displayed in Fig. 20.

For honeycomb samples, all water contaminations could be detected in delay and frequency evaluation; for Rohacell samples, detection was limited to delay mode. The differences in the penetrability of the cores influenced the visual detection of the water contents in delay mode. For the honeycomb structures, the contrast was best when looking at the signal that was reflected at the rear side of the core, where the absorption by the water content had the strongest influence on the image. The signal from the Rohacell samples on the other hand rather showed signs of the modified delay in the reflection in front of the core (see Fig. 21). The

THz radiation that passed the core twice was attenuated too much by the core structure itself already to discriminate the influence of the water contamination well.

Water inclusions are examples of a kind of defect that could be more efficiently detected if the measurements could be executed in transmission geometry. Since water is an excellent THz absorber, a patch of moisture in a sample will result in a zero-transmission area with good contrast to the dry surroundings, if the host material itself is not an extremely strong THz absorber (see example in Fig. 22).

4.5 Porosity

Another case of improved detectability in a transmission measurement was the highly porous laminate test sample. The detection of increased porosity (~4% of the volume) proved to be difficult with THz radiation. While effects of the enhanced porosity could be seen with the bare eye, and clearly in an ultrasonic image, the THz images did
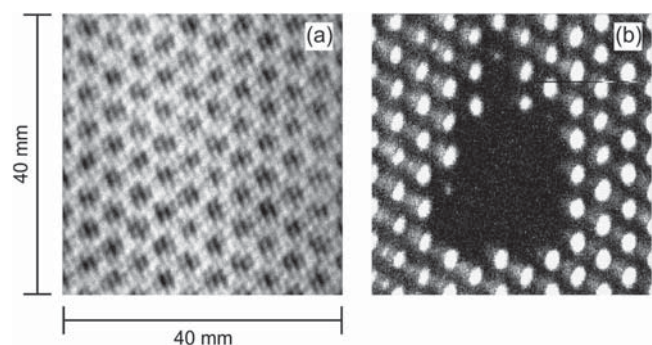

Fig. 22 The honeycomb C-sandwich sample from Fig. 20 with 0.75 ml water content evaluated in p2p mode; (a) reflection THz image of central area showing no signs of the water and (b) transmission THz image revealing the water volume via its strong THz absorption.
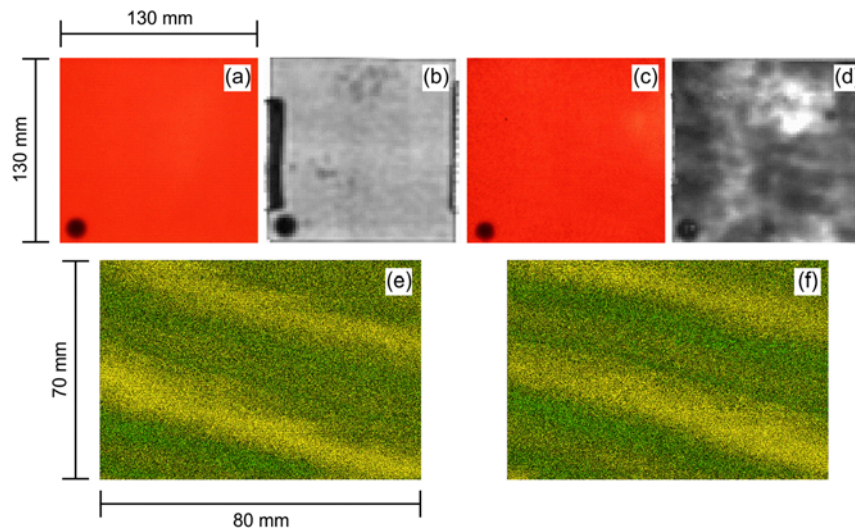
Fig. 23 Top row: translucent photographs and ultrasound pulse echo images of reference (a and b) and high-porosity (c and d) sample, indicating enhanced inhomogeneity through the porosity. Bottom row: delay image details of reference (e) and high-porosity (f) sample approximately 0.75 mm beneath the surface at 10-ps time delay.

not reflect an influence of the inhomogeneity within the high-porosity sample. The delay evaluation that allows peeking into the sample interior gave very similar results for both laminates, as can be seen in Fig. 23. Obviously, we cannot resolve the features that indicate elevated porosity in reflection.

However, the highly porous sample yielded more inhomogeneous, grainy images in p2p and frequency mode in comparison to the reference sample when both were measured in transmission (see the p2p images of Fig. 24).

4.6 Coating Misprocesses

Finally, for measurements of misprocessed coatings on CFRP panels, two different batches of samples were fabricated, one with PU and one with rain erosion (RE) coatings. Misprocesses included missing cleaning steps, deliberate contaminations with oil, release agent, water, or powder, processing without primer or with the wrong amount of primer, and application of the wrong amount of topcoat. THz-TDS lends itself to the analysis of coating misprocesses through changes in the propagation time of the THz radiation within the dielectric layers that are induced by the faults.
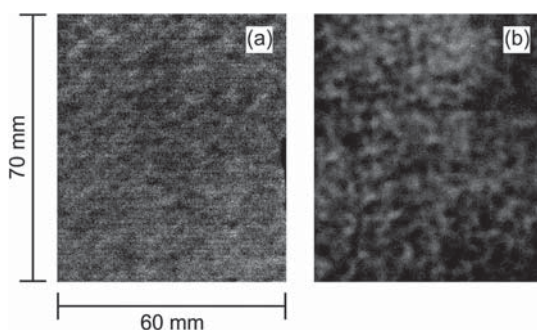

Fig. 24 Peak-to-peak THz images of reference (a) and high-porosity (b) sample taken in transmission measurements for comparison.

Our time-domain data traces always exhibited two main negative peaks that we identify with the coating surface reflection and the reflection at the CFPR substrate panel. The negative peaks are caused by the 180 deg phase shift from the reflection at an optically denser medium and the conductive panels, respectively. Unlike the weak and dispersion-broadened rear side reflection peaks from the GFRP samples, here the two peaks are comparable in amplitude and shape because the CFRP panels are conductive, and THz attenuation and dispersion in the coatings are low due to their limited thickness of a few 100 μm. The time difference between these two main peaks corresponds to twice the propagation time in the coating layer. Intermediate peaks can be caused by partial reflections at the interface between topcoat and primer. Examples can be seen in Fig. 25(c). In most cases of flawed coating examined by us, the propagation time showed a deviation from that measured on the respective reference sample, with the largest difference being caused by applying a too thick primer layer. Furthermore, a deliberate variation of the coating thickness translates into a proportional change in the propagation time within the coating layer [see Fig. 25(d)]. A more systematic examination of the delay variation that takes into account the dielectric properties of the different components of the coating layers (primer plus topcoat for PU coatings, two different primers plus topcoat for RE coatings) could be applied to gain a deeper understanding of the various processing flaws.

5 Conclusions and Outlook

We investigated the NDT inspection capabilities of THz-TDS on a wide choice of typical aeronautics composites with various defects. In most cases, it could be applied for detection. A-sandwiches and solid laminates yield a good detection rate for different defect types like debonds, delaminations, moisture ingress, and foreign material inclusions. Limited usability, besides the impossibility to directly visualize damages concealed by conductive carbon fibers, was found whenever a sandwich core, in particular
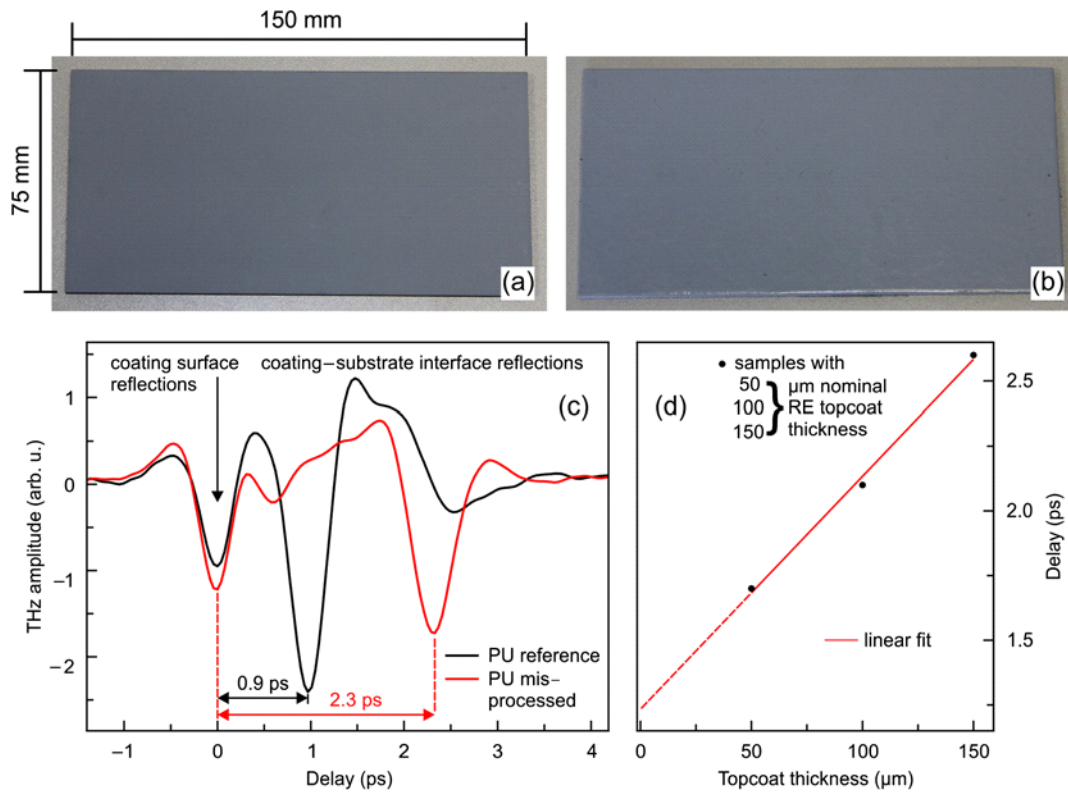
Fig. 25 Top row: photographs of reference CFRP panels with polyurethane [PU, (a)] and rain erosion [RE, (b)] coating. Bottom row: (c) time-domain traces recorded on PU-coated CFRP panels. The surface reflection has been shifted to zero delay for both datasets. The misprocessed sample with enhanced primer layer thickness shows a considerably longer propagation time of the THz pulses within the coating layer, as can be seen from the delay between surface and substrate reflection (secondary peaks). (d) Linear dependence of propagation time on topcoat thickness in RE samples; the zero thickness offset (1.23 ps) is caused by propagation in the primer layers of nominally constant thickness.

Rohacell foam, had to be penetrated twice. This affects especially thick C-sandwiches that are problematic structures for many NDT methods. It should be mentioned that tests with the fiber-coupled system showed improved penetration of sandwich and laminate structures because of its longer Rayleigh length compared to the reference system so that data from the whole sample volume could be gained. If lateral resolution can be traded off against the possibility to image the reflection from the opposite surface even in thick samples, softer focusing thus would be an option. Very promising is the possibility to analyze coating layers on CFRP panels with high depth resolution, which could not be done with any conventional NDT technique available in the project.

Now that the general applicability of THz-TDS for composites has been explored, the logical next steps are a detailed analysis of the results with respect to characteristic signatures of specific failure modes and a possible automatic identification of defects based on this. Such enhanced data processing and evaluation must be accompanied by steps to increase data acquisition speed and hardware improvements, e.g., the development of a robust and compact TDS transceiver sensor.

References

1. B. B. Hu and M. C. Nuss, "Imaging with terahertz waves," *Opt. Lett.* **20**(16), 1716–1718 (1995).
2. D. M. Mittleman, R. H. Jacobsen, and M. C. Nuss, "T-ray imaging," *IEEE J. Sel. Topics Quantum Electron.* **2**(3), 679–692 (1996).
3. D. M. Mittleman et al., "T-ray tomography," *Opt. Lett.* **22**(12), 904–906 (1997).
4. K. Kawase et al., "Non-destructive terahertz imaging of illicit drugs using spectral fingerprints," *Opt. Express* **11**(20), 2549–2554 (2003).
5. X. Wang et al., "Terahertz pulse reflective focal-plane tomography," *Opt. Express* **15**(22), 14369–14375 (2007).
6. C. Jördens and M. Koch, "Detection of foreign bodies in chocolate with pulsed terahertz spectroscopy," *Opt. Eng.* **47**(3), 037003 (2008).
7. W. Sun, X. Wang, and Y. Zhang, "A method to monitor the oil pollution in water with reflective pulsed terahertz tomography," *Optik* **123**(21), 1980–1984 (2012).
8. K. H. Jin et al., "High-speed terahertz reflection three-dimensional imaging for nondestructive evaluation," *Opt. Express* **20**(23), 25432–25440 (2012).
9. J. Xu et al., "T-rays identify defects in insulating-materials," in *Conf. Lasers and Electro-OpticsInternational Quantum Electronics Conference and Photonic Applications Systems Technologies, Technical Digest (CD)*, paper CMB2, Optical Society of America (2004).
10. N. Karpowicz et al., "Compact continuous-wave subterahertz system for inspection applications," *Appl. Phys. Lett.* **86**(5), 054105 (2005).
11. C. D. Stoik, M. J. Bohn, and J. L. Blackshire, "Nondestructive evaluation of aircraft composites using transmissive terahertz time domain spectroscopy," *Opt. Express* **16**(21), 17039–17051 (2008).
12. C. Stoik, M. Bohn, and J. Blackshire, "Nondestructive evaluation of aircraft composites using reflective terahertz time domain spectroscopy," *NDT&E Int.* **43**(2), 106–115 (2010).
13. A. Cooney and J. L. Blackshire, "Advanced imaging of hidden damage under aircraft coatings," *Proc. SPIE* **6179**, 617902 (2006).
14. R. Anastasi and E. I. Madaras, "Terahertz NDE for under paint corrosion detection and evaluation," in *4th Int. Workshop Ultrasonic and Advanced Methods for Nondestructive Testing and Material Characterization*, http://www.ndt.net/article/v11n07/papers/05.pdf (10 October 2013).

15. N. Karpowicz et al., "Fire damage on carbon fiber materials characterized by THz waves," *Int. J. High Speed Electron. Syst.* **17**(2), 213–224 (2007).
16. F. Destic et al., "THz QCL-based active imaging dedicated to nondestructive testing of composite materials used in aeronautics," *Proc. SPIE* **7763**, 776304 (2010).
17. I. Amenabar, F. Lopez, and A. Mendikute "In introductory review to THz non-destructive testing of composite mater," *J. Infrared Milli. Terahz. Waves* **34**(2), 152–169 (2013).
18. E. Cristofani et al., "Assessment of 3-D signal and image processing using FMCW THz signals," *Proc. of the OPTRO*, http://www.sic.rma.ac.be/~ecristof/DOTNAC_pub/OPTRO2012_final.pdf (2012).
19. F. Tauser et al., "Electronically controlled optical sampling using 100 MHz repetition rate fiber lasers," *Proc. SPIE* **6881**, 68810O (2008).

Frank Ospald is a postdoctoral researcher in the Ultrafast Photonics and THz Physics group at the University of Kaiserslautern, Germany. He graduated in physics at the LMU Munich and received his PhD from the University of Kaiserslautern for work on fast photoconductive switches pumped at 1560 nm for THz research and applications, which was carried out at the MPI for Solid State Research in Stuttgart. He focuses on the development of fiber laser-based mobile THz systems for spectroscopy and materials testing in close cooperation with the Fraunhofer Institute for Physical Measurement Techniques IPM.

René Beigang is a professor for experimental physics and head of the Ultrafast Photonics and THz Physics group at the University of Kaiserslautern. He started his scientific career in the field of laser physics, nonlinear optics, atomic physics, and generation and application of ultrashort laser pulses. He has been working in the field of THz spectroscopy and applications for more than a decade.

Joachim Jonuscheit is a business development manager and deputy head of department in the "Materials Characterization and Testing" (MC) department of the Fraunhofer Institute for Physical Measurement Techniques IPM. He graduated in physics at the Ludwig-Maximilians University of Munich and received his PhD degree from the University of Erlangen-Nuremberg. He worked at various laser companies for several years in several management positions (project manager, R&D manager, and production manager).

Patrick Mounaix received the degree of Engineer of Material Science in 1988 from the Ecole Universitaire D'Ingénieur de Lille (EUDIL) and the third cycle thesis on quantum devices in 1992 from the University of Lille (PhD). Then he joined CNRS and the High Frequency Department of the Institut-d'Electroniqueet de Micro-électronique du Nord (IEMN). He moved to Bordeaux in 2002, where he developed a new terahertz spectroscopy activity. Now he is currently interested in equilibrium and time-resolved terahertz spectroscopy techniques for solid and liquid materials and terahertz imaging applications, chiefly computer tomography for art and NDE industrial applications.

Pablo Venegas has graduated as an industrial engineer and has more than 7 years of experience in the aeronautical sector in the research and development of thermographic techniques applied as NDT tools. He has a master's degree in investigation in industrial technologies and is now a PhD student. He has been working in The Aeronautical Technologies Centre as a project manager for more than 6 years, where he has gained experience in national and European projects in the investigation of the thermographic technology as well as in the evaluation and validation of new NDT techniques. At the beginning of 2013, he has become head of NDT area in The Aeronautical Technologies Centre.

Laura Vega has graduated as an industrial engineer and has more than 5 years of experience in the aeronautical sector in the research and development of thermographic techniques applied as NDT tools. She has a master's degree in investigation in industrial technologies and is now a PhD student. She has been working in The Aeronautical Technologies Centre as a project engineer for more than 5 years, where she has gained experience in national and European projects in the investigation of the thermographic technology as well as in the evaluation and validation of new NDT techniques.

Ion López has graduated from E.T.S.I. of Bilbao as industrial engineer and was a PhD student at the University of Cantabria. He has been working as head of Singular Projects at CTA (Aeronautical Technologies Centre) since 2008, participating in different certification test campaigns for the aeronautical sector and different R&D projects. He has been involved as project manager in several structural test projects related to different aircraft models (A320, A340, A380 and A400M). His main research domains are combustion and scale model fire tests and infrared thermography as NDT technique for defect detection.

Marijke Vandewal graduated in 1996 from the Royal Military Academy, division Polytechnics, specialty Telecommunications. After a specialized avionics Air Force training, she was assigned at the flight Avionics in Kleine Brogel (Belgium), an F-16 Air Force Base. Then she was transferred to Brussels as a software engineer on C-130 transport aircraft. In 2000, she became an assistant at the Royal Military Academy, in optronics, radar, and microwave techniques. In cooperation with DLR (Deutsches Zentrum für Luft- und Raumfahrt) she obtained her PhD degree in engineering sciences in 2006. Since 2008, she has been teaching as a military professor at the Department CISS (communication, information, systems and sensors) of the Royal Military Academy.

Biographies and photographs of other authors not available.